Delft University of Technology

Enhanced kinetic energy entrainment in wind farm wakes
Large eddy simulation study of a wind turbine array with kites

Ploumakis, Evangelos; Bierbooms, Wim

DOI
10.1007/978-981-10-1947-0_8

Publication date
2018

Document Version
Final published version

Published in
Green Energy and Technology

Citation (APA)
Ploumakis, E., & Bierbooms, W. (2018). Enhanced kinetic energy entrainment in wind farm wakes: Large eddy simulation study of a wind turbine array with kites. In *Green Energy and Technology* (9789811019463 ed., pp. 165-185). (Green Energy and Technology; No. 9789811019463). Springer. https://doi.org/10.1007/978-981-10-1947-0_8

Important note
To cite this publication, please use the final published version (if applicable).
Please check the document version above.

Copyright
Other than for strictly personal use, it is not permitted to download, forward or distribute the text or part of it, without the consent of the author(s) and/or copyright holder(s), unless the work is under an open content license such as Creative Commons.

Takedown policy
Please contact us and provide details if you believe this document breaches copyrights.
We will remove access to the work immediately and investigate your claim.

This work is downloaded from Delft University of Technology.
For technical reasons the number of authors shown on this cover page is limited to a maximum of 10.

Chapter 8
Enhanced Kinetic Energy Entrainment in Wind Farm Wakes: Large Eddy Simulation Study of a Wind Turbine Array with Kites

Evangelos Ploumakis and Wim Bierbooms

Abstract Wake effects in wind farms are a major source of power production losses and fatigue loads on the rotors. It has been demonstrated that in large wind farms the only source of kinetic energy to balance the energy extracted by the turbines is the vertical transport of the free-stream flow kinetic energy from above the wind turbine canopy. This chapter explores the possibility to enhance this transport process by introducing kites in steady flight within a small wind turbine array. In a first step, an array of four wind turbines, aligned with the streamwise velocity component, is simulated within a large eddy simulation framework. The turbines are placed in a pre-generated turbulent atmospheric boundary layer and modeled as actuator disks with both axial and tangential inductions, to account for the wake rotation. In a second step an identical turbine configuration with interspersed kites is investigated. The kites are modeled as body forces on the flow, equal in magnitude and opposite in direction to the vector sum of the lift and drag forces acting on the kite surfaces. A qualitative comparison of the mean flow statistics, before and after the introduction of the kites is presented.

8.1 Introduction

Humanity has harnessed the power of the wind for thousands of years, initially through sails and windmills. For more than two thousand years wind-powered machines had been used to pump water and grind grain. By the end of the 19th century pioneers such as Danish scientist, inventor and educator Poul la Cour employed wind energy for generating electricity. Since these days wind energy has progressed

Evangelos Ploumakis (✉) · Wim Bierbooms
Delft University of Technology, Faculty of Aerospace Engineering, Kluyverweg 1, 2629 HS Delft, The Netherlands
e-mail: eploumakis@yahoo.gr, w.a.a.a.bierbooms@tudelft.nl

© Springer Nature Singapore Pte Ltd. 2018
R. Schmehl (ed.), *Airborne Wind Energy*, Green Energy and Technology, https://doi.org/10.1007/978-981-10-1947-0_8

from being a minor source of electricity to covering 10.2% of the EU's consumption in 2014 [1].

With the rapidly growing global wind energy capacity an increasing number of wind turbines has been installed in large wind farms. These farms are usually organized in patterns of rows and columns and the array configuration is typically chosen according to the dominant wind direction and turbine size. Because of the varying wind direction most turbines in such an array are exposed to the wakes of upstream turbines which leads to significant power losses. For example at Horns Rev, one of the first large-scale offshore wind farms in the world, power losses of more than 40% for certain wind directions have been reported [4]. The wake flows are also associated with increased turbulence levels and higher fatigue loads for exposed turbines. On the other hand, the increased turbulence enhances the flow entrainment from the free stream above the wind turbine canopy, leading to a faster wake recovery and more kinetic energy available for harnessing by downwind turbines. A visualization of simulated turbine wakes in a wind farm is shown in Fig. 8.1.

As wind farms grow larger the asymptotic limit of the fully developed flow inside the farms has been receiving a lot of interest. With the height of the atmospheric boundary layer (ABL) of about 1 km and modern wind farms exceeding 10–20 km in the horizontal direction a fully developed flow regime can be established [21].

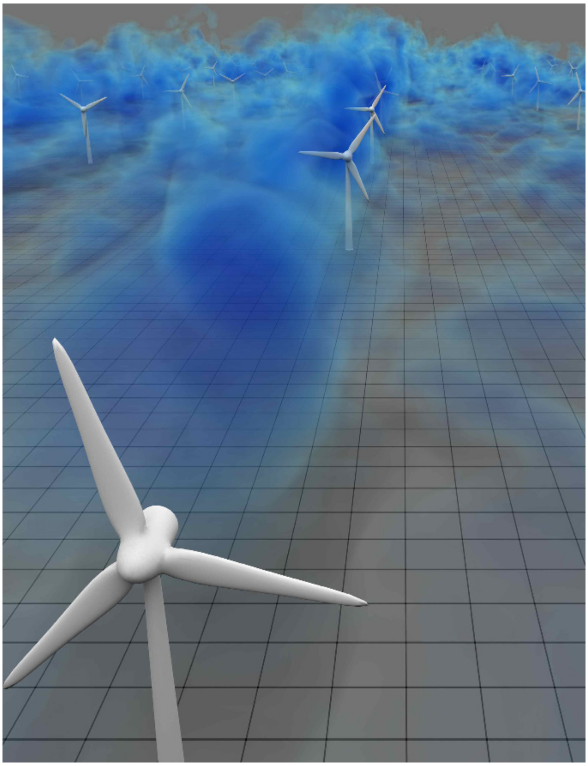

Fig. 8.1 Simulated wind farm turbulence: volume rendering of low-velocity wake regions. Visualization generated by D. Bock, National Center for Supercomputing Applications, XSEDE, based on wind farm LES data [26, 27]

This limit state is associated with wind farms on flat terrain whose length exceed the height of the ABL by more than an order of magnitude [9].

From a physical point of view it is important to understand that for large wind turbine arrays entrainment of kinetic energy from the undisturbed flow plays an important role in replenishing the wake. For stand-alone wind turbines the extracted power is related to the difference between the upstream and downstream kinetic energy fluxes. On the contrary, it is shown that for the turbines, operating in a fully developed wind turbine boundary layer, the entrainment of kinetic energy from the free atmosphere into the wind turbine canopy is the only source of kinetic energy to balance that extracted by the wind turbines [8]. The total kinetic energy that is available in the lower parts of the ABL is therefore extracted in two primary ways: from the incoming wind at the leading edge of the wind farm and from above the wind farm [20]. Changes in the streamwise direction can be neglected after the fourth row of turbines and vertical transport of momentum becomes a crucial parameter in determining the overall efficiency of infinitely large wind farms [4].

In view of the realization that for large wind farms it is the vertical entrainment that dominates the availability of power an innovative way to enhance the vertical transport of momentum is proposed. The study of new designs that could potentially assist the wake re-energizing process in wind turbine arrays is a crucial part of the ongoing quest to improve the overall efficiency and lower the cost of energy. In the present study, the possibility to enhance the vertical transport of momentum by introducing kites in steady flight within a wind turbine array is investigated. This concept is visualized in Fig. 8.2. Large eddy simulations (LES) of a small wind

Fig. 8.2 Visualization of the proposed flow entrainment based on interspersed kites [6]

turbine array operating in a turbulent ABL are used to evaluate the effect of the kites on the mean flow statistics.

In Sect. 8.2 the modeling approaches for the simulation of the ABL, the wind turbines and the kites in the computational domain are presented. In Sect. 8.3 an LES of a row of four wind turbines is presented and discussed, while in Sect. 8.4 the same configuration with interspersed kites is analyzed. The main point of interest is the effect of the kites on the recovery characteristics of the wake flow. The preliminary content of the present chapter has been presented at the Airborne Wind Energy Conference 2015 [23] and is published as MSc thesis [22].

8.2 Numerical Setup and Modeling Considerations

Modeling of a wind turbine wake is a key task for the energy yield prediction of operating wind farms as well as the optimization of new wind farm layout configurations. Numerical simulations, instead of experiments, are the focus of scientific research for two main reasons. Full-scale, high-quality experiments are costly and are limited to provide information on the flow field. Wind flow modeling software is nowadays mainly used to extrapolate the flow field data from on-site measurements to locations where poor or no measurements were taken. Most of the modeling software used is based on either micro-scale models derived from measurement campaigns, such as used in WAsP [13], WindPRO [14] and WindFarmer [11], or on computational fluid dynamics (CFD) where the differential governing equations of fluid motion are solved numerically.

8.2.1 Atmospheric Boundary Layer Modeling

When performing CFD simulations a key issue for wind engineers is the accurate representation of the turbulent ABL. Compared to standard Reynolds-averaged-Navier-Stokes (RANS) simulation, LES is generally known to reproduce main turbulence properties with higher accuracy, though it is stressed that further research is needed in sub-grid scale modeling [10, 31]. One of the major difficulties encountered in LES is the definition of realistic upstream conditions at the domain inlet. Several inflow generation techniques have been proposed in the past decade and can be classified into three main categories: synthetic methods, precursor simulations and recycling methods as classified by Keating et al. [16]. To generate the turbulent inflow, also denoted as "numerical wind", the LES model coupled with the Smagorinsky-Lilly sub-grid-scale (SGS) model available in Fluent®was used. More realistic inflow turbulence, with better spatial and temporal correlations, is achieved by running a precursor simulation either before the main simulation or simultaneously with it, usually by extending the domain upstream the area of interest.

A set of general simplifications were considered necessary to make numerical simulations of the ABL possible within the LES framework. Firstly, the ABL is considered neutrally stable meaning that thermal effects are neglected. Since the purpose of the study is to provide a qualitative report of the examined test cases, the assumption of a neutral ABL saves computational time since the additional equation for the transport of potential temperature does not need to be solved. Secondly, the flow is considered to be incompressible, which is valid for low Mach number ($M < 0.3$), at which the flow is quasi-steady and isothermal. For the relatively low wind speeds ($< 20\,\mathrm{m/s}$), typically encountered in our simulations, we can expect minimal compressibility effects on the solution therefore the assumption to keep the density constant in space and time.

In order to generate the fluctuating velocity components in the computational domain the spectral synthesizer method in Fluent®is employed. The synthesized turbulence method is used in our case, to provide an initial perturbation to our LES of turbulent flow and initiate turbulent motions in the flow. For a velocity inlet boundary condition, a random field of fluctuating velocities, based on a random flow generation (RFG) Fourier technique proposed by Smirnov, Shi et al. [25], is superimposed on a specified mean velocity.

The numerical wind field was generated by a precursor simulation in an empty domain without any wind turbines or kites. In this simulation the pressure-driven flow is recycled in the domain allowing the boundary layer and its turbulence to develop naturally. Once the flow approaches the logarithmic profile of the predefined mean velocity

$$\overline{U} = \frac{u_*}{k} \ln\left(\frac{z}{z_0}\right), \tag{8.1}$$

where z_0 denotes the aerodynamic roughness length, $k = 0.4$ the von Karman constant and u_* the friction velocity, the three velocity components are captured at a specified vertical plane. The friction velocity u_* is related to the level of turbulence in the surface layer, the bottom 5–10% of the mixing layer in which the turbulence is mostly mechanically generated, and typically increases with higher values of the surface roughness z_0.

8.2.2 Rotor Modeling

Simulations of the physical rotor are computationally very expensive because of the fine computational mesh that is required to adequately resolve the different parts of the rotor and the generated flow structures. It is also clear that the high resolution of the near wake is not of major importance when studying the flow in large-scale wind farms. Thus, when modeling wind turbine arrays with CFD, the actuator disk [2, 19] and the actuator line [28, 29] methods are typically used, the actuator surface [12] method has only been recently explored.

Rankine (1865) and Froude (1889) have used one-dimensional momentum theory to predict the performance of ship propellers, later Betz (1919) applied this actuator disk model to assess the energy extraction potential of wind turbines. The theory is depicted in Fig. 8.3 which shows a stream tube that is expanding in flow direction. This expansion effect is caused by the flow resistance of the actuator disk

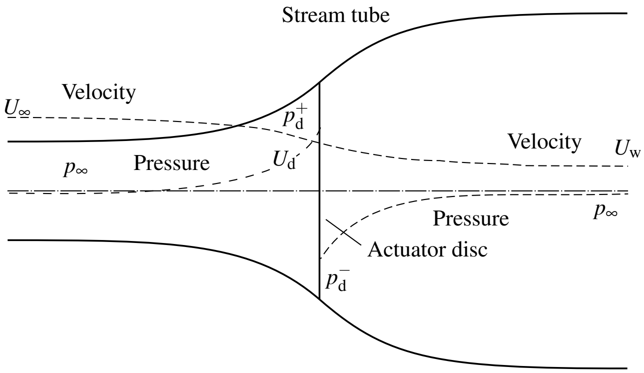

Fig. 8.3 Schematic of the flow passing through the wind turbine rotor modeled as an actuator disk, adapted from [7]

which introduces a pressure drop in the flow. The force that the actuator disk exerts on the flow is added to the momentum equation

$$\frac{D\mathbf{u}}{Dt} = \mathbf{f} - \frac{\mathbf{1}}{\rho}\nabla\mathbf{p} + \nu\nabla^{\mathbf{2}}\mathbf{u}. \tag{8.2}$$

The thrust force acting on the wind turbine can also be expressed as the summation of forces acting on both sides of the actuator disk, calculated from the pressure difference across the disk as

$$T = A_\mathrm{d}(p_\mathrm{d}^+ - p_\mathrm{d}^-), \tag{8.3}$$

where $A_\mathrm{d} = \pi D^2/4$ denotes the surface area of the actuator disk. Normalization with the dynamic pressure in the flow leads to the non-dimensional thrust coefficient

$$C_\mathrm{T} = \frac{T}{\frac{1}{2}\rho U_\infty^2 A_\mathrm{d}}. \tag{8.4}$$

However, in LES of wind turbine arrays with significant wind turbine wake interactions the upstream reference velocity U_∞ is not readily known. It is therefore more natural to use the velocity normal to the rotor disk, U_d, to calculate the thrust coefficient at the disks. The thrust force in our simulations is expressed in terms of a modified thrust coefficient [9],

$$C_\mathrm{T}' = \frac{C_\mathrm{T}}{(1-a)^2}, \tag{8.5}$$

introducing the axial induction factor a as the fractional decrease in wind velocity between the free stream, U_∞, and the rotor plane, U_d, as

$$a = \frac{U_\infty - U_\mathrm{d}}{U_\infty}. \tag{8.6}$$

When representing the turbine rotor by an actuator disk the axial induction factor a is closely related to the power extracted by the wind turbine. In case the wind approaching the turbine is brought to rest ($a = 1$) no power will be extracted by the wind turbine since there will be no flow through the rotor plane. Also, if there is no change in the velocity of the wind passing through the rotor ($a = 0$) no power will be extracted since the kinetic energy of the air before and after the turbine blades remains unchanged. For negative values of the induction factor ($a < 0$) the wind turbine rotor acts as a propeller instead of a generator. The induction factor is related to the power coefficient, $C_\mathrm{P} = 4a(1-a)^2$, and thrust coefficient, $C_\mathrm{T} = 4a(1-a)$, of a turbine. For an induction factor of $a = 1/3$ one can obtain the maximum power and thrust coefficients of an ideal wind turbine rotor. This condition is well known as the "Betz limit" defining the maximum fraction of kinetic energy that can be extracted from the flow and converted into usable power. It can be shown analytically that this maximum conversion efficiency is $16/27$ (59.3%) independent of the design of the rotor.

Combining Eqs. (8.4) and (8.5) the thrust force is calculated on the basis of the modified thrust coefficient C_T' as

$$T = -\frac{1}{2}\rho C_\mathrm{T}' U_\mathrm{d}^2 A_\mathrm{d}. \tag{8.7}$$

For flows with significant three-dimensional effects the tangential and radial velocities need to be taken into account to generate swirl in the flow. The induced radial velocity is typically small compared to the axial and tangential velocities and is therefore often neglected in calculations. The tangential velocity is calculated as $U_\theta = U_x \cos\theta + U_y \sin\theta$, where U_x and U_y are the instantaneous velocities in x- and y-direction and θ is the angular coordinate. The change in tangential velocity is expressed in terms of a tangential flow induction factor

$$a' = \frac{1-3a}{4a-1}. \tag{8.8}$$

The tangential velocity varies along the span of the blades and accordingly is a function of the radial position r. Upstream of the rotor disk the tangential velocity vanishes while immediately downstream the tangential velocity magnitude is $2\omega r a'$, where ω is the angular speed of the rotor. Since it is a reaction of the flow to the motion of the rotor its direction is always opposing the direction of rotation.

Variants of the actuator disk model (ADM) discussed in literature account for thrust and tangential forces (ADM-R) while others account only for thrust forces (ADM-NR). The ADM may simulate wind turbines and the induced wakes but fails to create the tip vortices carried onto the wake [28]. Wu and Porté-Agel [33] compared LES simulations of a wind farm using the ADM-NR and ADM-R approaches with field measurements. It was concluded that the ADM-R yields improved predictions in the wake compared to the ADM-NR which stresses the importance of turbine-induced flow rotation for the accurate prediction of the wake structures. The present study uses the ADM approach with both axial and tangential inductions.

8.2.3 Modeling the Kites

By definition an aerodynamic lifting device uses the relative velocity between wind field and flying device, quantified by the apparent wind velocity vector

$$\mathbf{v}_\mathrm{a} = \mathbf{v}_\mathrm{w} - \mathbf{v}_\mathrm{k}, \tag{8.9}$$

to generate a force component perpendicular to $\mathbf{v}_\mathrm{a}$, denoted as lift force

$$L = \frac{1}{2}\rho C_\mathrm{L} v_\mathrm{a}^2 A_\mathrm{k}, \tag{8.10}$$

and a force component aligned with $\mathbf{v}_\mathrm{a}$, denoted as drag force

$$D = \frac{1}{2}\rho C_\mathrm{D} v_\mathrm{a}^2 A_\mathrm{k}. \tag{8.11}$$

In these equations, the parameter A_k denotes the projected wing surface area, while C_L and C_D denote the aerodynamic lift and drag coefficients. Both force components constitute the resultant aerodynamic force $\mathbf{F}_\mathrm{a} = \mathbf{L} + \mathbf{D}$ with magnitude

$$F_\mathrm{a} = \frac{1}{2}\rho C_\mathrm{R} v_\mathrm{a}^2 A_\mathrm{k}. \tag{8.12}$$

Accordingly, the resultant aerodynamic coefficient is given by

$$C_\mathrm{R} = \sqrt{C_\mathrm{L}^2 + C_\mathrm{D}^2} = C_\mathrm{D}\sqrt{1 + \left(\frac{L}{D}\right)^2}. \tag{8.13}$$

Because the resultant aerodynamic force $\mathbf{F}_\mathrm{a}$ acts on the flying vehicle, the reaction force $-\mathbf{F}_\mathrm{a}$ reversely acts on the flow, causing its retardation and deflection.

These fundamental aerodynamic relationships are illustrated schematically in Fig. 8.4 for the cases of untethered gliding flight of a wing at $v_\mathrm{w} = 0$ (left), tethered flight at $l_\mathrm{t} = \mathrm{const.}$ and $v_\mathrm{k} > 0$ (center) and tethered flight at $l_\mathrm{t} = \mathrm{const.}$ and $v_\mathrm{k} = 0$ (right). The glide angle ε is defined on the basis of the depicted case of untethered gliding flight as the angle measured from the horizontal plane to the flight velocity vector $\mathbf{v}_\mathrm{k}$ or, equivalently, to the apparent wind velocity vector $\mathbf{v}_\mathrm{a} = -\mathbf{v}_\mathrm{k}$. Because $\mathbf{F}_\mathrm{a}$ is perpendicular to the horizontal plane and $\mathbf{L}$ is perpendicular to $\mathbf{v}_\mathrm{k}$, the angle ε also characterizes the tilt rotation of the lift vector from the vertical, which

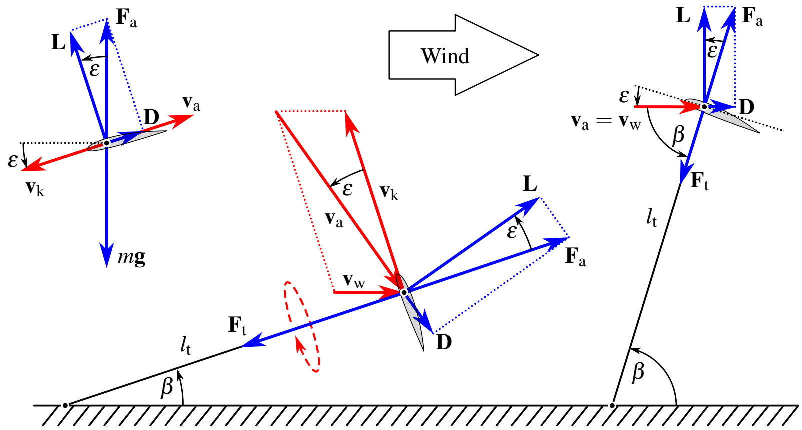

Fig. 8.4 Velocity vectors (red) and force vectors (blue) for an untethered wing in steady gliding flight at $v_k = 0$ (left), for a massless kite exposed to a wind velocity and flying at constant tether length l_t in a continuous loop (center) and at a static position (right), adapted from [15]. The elevation angle β is measured from the ground plane to the tether. The two tethered configurations depict the special case in which the tether and the wind velocity $\mathbf{v}_w$ are in the illustration plane

leads to following relationships between kinematic properties and force components

$$\frac{1}{\tan\varepsilon} = \frac{L}{D}, \tag{8.14}$$

$$\frac{1}{\sin\varepsilon} = \sqrt{1 + \left(\frac{L}{D}\right)^2}. \tag{8.15}$$

These imply that the gliding angle ε depends only on the lift-to-drag ration L/D of the wing and is unaffected by its mass m. By analyzing the vertical equilibrium between aerodynamic force $\mathbf{F}_a$ and gravitational force $m\mathbf{g}$ we can find the gliding velocity v_k of the wing as a function of its mass. We find that the heavier the wing, the faster it descends on the straight gliding trajectory described by the angle ε.

Tethered flight introduces an additional tether force $\mathbf{F}_t$ which, in contrast to the gravitational force, is not constant but adjusts itself to the aerodynamic performance and flight mode of the wing. Especially when the wind velocity v_w or the flight velocity v_k are high, the wing experiences a high apparent wind velocity v_a according to Eq. (8.9) and, as consequence, the steady force equilibrium is dominated by the aerodynamic force $\mathbf{F}_a$, calculated from Eq. (8.12), and the induced tether force $\mathbf{F}_t$. This condition is also typical for fabric membrane wings with a low mass m and for this reason we simplify the analyses of tethered flight by neglecting the gravitational force.

Loyd [18] was among the first to recognize the potential of kites to produce large traction forces that can be used for energy generation with a minimal material effort. In his analysis he distinguishes the two different modes of operation that are schematically illustrated in Fig. 8.4 for the special case of constant tether length. Loyd concludes that operation in crosswind maneuvers, as illustrated in Fig. 8.4 (center), achieves by far larger tether forces than flight at a static position, as shown in Fig. 8.4 (right). It can be shown that for operation in crosswind flight maneuvers at an elevation angle β the apparent wind speed is calculated by [15, 24]

$$v_\mathrm{a} = v_\mathrm{w} \cos\beta \sqrt{1 + \left(\frac{L}{D}\right)^2} = v_\mathrm{w} \frac{\cos\beta}{\sin\varepsilon}. \tag{8.16}$$

In this equation the angle ε is used to quantify the lift-to-drag ratio according to Eq. (8.15) in generalization of the original kinematic definition for steady gliding flight. When the force equilibrium is dominated by $\mathbf{F}_\mathrm{a}$ and $\mathbf{F}_\mathrm{t}$, the angle ε can be interpreted kinematically as the angle between the tether normal plane and the apparent wind velocity vector $\mathbf{v}_\mathrm{a}$. Equation (8.16) shows that the apparent wind velocity and with this also the aerodynamic force according to Eq. (8.12) are maximum for a horizontal tether ($\beta = 0$) and decreasing for increasing elevation angle. For this reason, the elevation angle can be used as an operational parameter to adjust the generated traction force of the kite and the resulting flow deflection towards the ground. The equation further indicates the substantial increase of v_a and F_a with increasing L/D.

For $v_\mathrm{k} = 0$, the kite assumes a static position with β reaching its maximum value, v_a its minimum value

$$v_\mathrm{a} = v_\mathrm{w}, \tag{8.17}$$

and, consequently, also the aerodynamic force F_a reaching its minimum value. The steady force equilibrium illustrated in Fig. 8.4 (right) leads to

$$\tan\beta = \frac{L}{D}, \tag{8.18}$$

$$\cos\beta = \frac{1}{\sqrt{1 + \left(\frac{L}{D}\right)^2}}. \tag{8.19}$$

For $v_\mathrm{k} \to 0$, Eq. (8.16) converges towards Eq. (8.17), which can be shown by inserting the limiting value of $\cos\beta$ given by Eq. (8.19) into Eq. (8.16).

From the above considerations we can conclude that the statically positioned kite can be used as a baseline solution to deflect the flow from the free stream towards the ground. For example, by assuming a glide angle of $\varepsilon = 10°$, which corresponds to a lift-to-drag ratio of $L/D = 5.67$, we can use Eq. (8.18) to calculate the elevation angle of $\beta = 80°$ for static flight. To further increase the traction force the kite can be flown in crosswind flight maneuvers at lower elevation angles. This technique, which requires additional flight control subsystems for the kites, will be used in Sect. 8.4 to intensify the entrainment of flow from the free stream.

To quantify the flow entrainment effect of the kite we define the kite power density as the product of aerodynamic force F_a and apparent wind velocity v_a divided by the projected wing surface area A_k,

$$P' = \frac{F_a v_a}{A_k}. \tag{8.20}$$

It should be noted that this definition differs from the traction power density, which is based on the reeling velocity v_t of the tether [24].

Because the geometrical dimensions of the kites by far exceed the resolution of the computational mesh they are taken into account in the flow simulations as discontinuous pressure jumps over infinitely thin surfaces specified as a function of the instantaneous inflow velocity. The aerodynamic characteristics of a three-dimensional wing section of a ram-air kite were obtained from de Wachter [30] who performed measurements of the inflated wing shape in a wind tunnel using photogrammetry and laser scanning, followed by CFD analysis of the flow past the determined shape. The computed pressure distribution is used to determine the total force on the flow for each kite. The pressure difference between the upper and lower surfaces of the wing is translated into a resultant aerodynamic force that is decomposed into lift and drag force components. The resultant aerodynamic coefficient is evaluated by numerical integration of the pressure difference between the upper and lower wing surfaces over the chord c

$$C_R = \frac{1}{c}\int_0^c \left(C_{p,l} - C_{p,u}\right) dx. \tag{8.21}$$

8.3 Numerical Simulations of an Array of Four Wind Turbines

In this section we present numerical simulations for a wind turbine array in a neutral ABL using the LES framework available in the CFD solver Fluent®. The velocity profiles generated in the precursor simulation are used as inflow conditions for all wind turbine simulations. The turbines are arranged along the main flow direction as illustrated in Fig. 8.5. To model the effect of the wind turbines on the flow field we use the fan boundary condition, which is formulated as a discontinuous pressure jump across an infinitely thin surface and is specified as a function of the normal velocity at the actuator discs. Accordingly, the thrust force of each turbine is calculated from Eq. (8.7) and applied to the flow field as indicated in Fig. 8.5. More details of this procedure are available in [22, Sect. 6-1-1]. The employed ADM-R approach accounts for both axial and tangential inductions and allows for an accurate prediction of the wind turbine wakes at a reasonable computational cost [2, 19]. The wake flow characteristics are the main focus of this study.

The effect of wind turbine loading on wake evolution is studied by applying two different thrust coefficients, corresponding to sub-optimal and to optimal loading of the turbines. The sub-optimal loading, also denoted as partial loading, is defined by $C_T' = 0.85$ and $a = 0.17$ while the optimal loading is defined by $C_T' = 2$ and

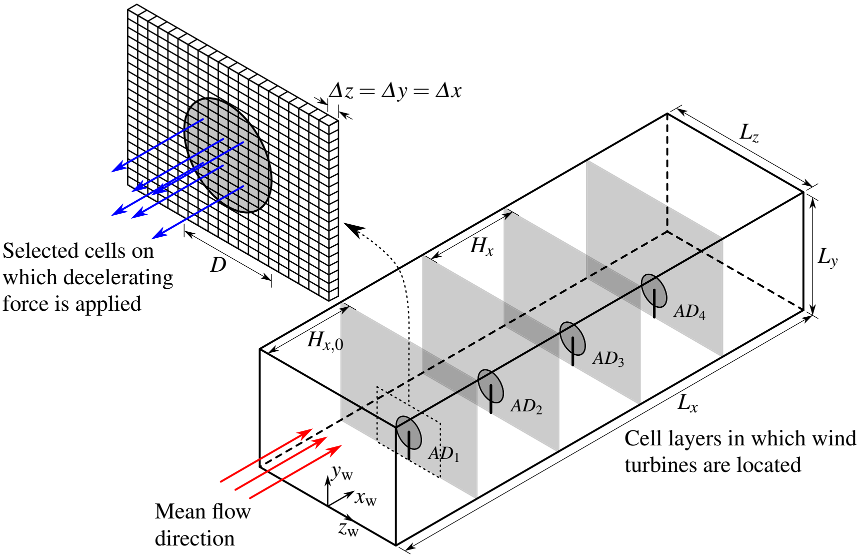

Fig. 8.5 Schematic view of the computational domain (not to scale) with the actuator disks AD_1, AD_2, AD_3 and AD_4 arranged along the main flow in x_w-direction, modified from [17]

$a = 0.33$. For smaller thrust coefficients the performance of the upstream turbines is sub-optimal which allows the downstream turbines to capture more power. Sub-optimal power extraction has already been treated in the literature with the aim to coordinate wind turbine controllers to optimize wind farm performance [3, 5]. This mode of operation was developed to account for the aerodynamic coupling by wake interaction in a group of turbines to maximize the total captured power. The geometry and mesh parameters are summarized in Table 8.1.

Table 8.1 Geometry and mesh parameters for the considered turbine load cases $C'_T = 0.85$ and $C'_T = 2$. The total number of mesh nodes is 2,894,441

Parameter name	Symbol	Value	Unit
Number of turbines	N	4	
Diameter actuator disks	D	80	m
Hub height	H_h	80	m
Inter-turbine spacing	H_x	$6D$	
Inflow section length	$H_{x,0}$	$4D$	
Length flow domain	L_x	$28D$	
Width flow domain	L_y	$10D$	
Height flow domain	L_z	$10D$	
Cell size	$\Delta x, \Delta y, \Delta z$	$D/10$	

The size of the flow domain is identical to the one used to generate the wind profiles in the precursor simulation. The wind reference frame x_w, y_w, z_w depicted in Fig. 8.5 is used to describe absolute positions in the flow domain. A uniform cell size is chosen as compromise between the required resolution of the relevant large vortex structures and the computational cost. In general, three-dimensional unsteady LES is computationally demanding and to finish within a practical timeframe the simulations need to be processed in parallel on high-performance computer clusters. Using 20 Intel®Xeon®CPU E5-2670v2 cores with 4GB of RAM per core, the time required to compute the flow statistics for a sample domain of $8 \times 8 \times 8$ cells was approximately 100 hours.

Results are presented in the normalized local reference frames $x/D, y/D, z/D$ of the individual turbines. The streamwise coordinates x/D are defined such that $x/D > 0$ refers to positions downstream and $x/D < 0$ to positions upstream of the respective turbine. The wake flow is characterized by vertical profiles of the mean streamwise velocity and the kinetic energy flux at relative downstream positions $x/D = 5$. In general, a higher wind turbine loading is associated with a larger thrust coefficient C'_T and increased energy extraction from the wind. This reduces the kinetic energy in the wake flow which can be recognized from the velocity profiles of the load cases $C'_T = 2$ and 0.85 illustrated in Fig. 8.6.

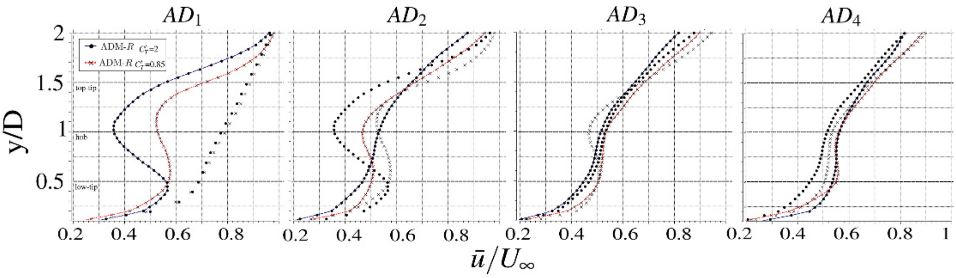

Fig. 8.6 Vertical profiles of the normalized streamwise velocity. The profiles represented by lines and symbols are computed at turbine downstream locations $x/D = 5$. The profiles represented only by symbols are computed at turbine upstream locations $x/D = -1$, with crosses denoting the load case $C'_T = 2$ and dots the load case $C'_T = 0.85$. The maximum tip height of the wind turbines is at $y/D = 1.5$, the hub height at $y/D = 1$ and the minimum tip height at $y/D = 0.5$

The wake velocity recovery reveals the gradual development of the flow towards an equilibrium state as it develops along the wind turbine array. As expected, the wake of actuator disk AD_1 shows a more pronounced velocity deficit for higher turbine loading. From AD_2 onwards the wake velocity recovers much faster, as can be seen when comparing the upstream velocity profiles at $x/D = -1$, represented by only symbols, with the downstream profiles at $x/D = 5$, represented by symbols and lines. For AD_3 and AD_4 the simulations predict a complete recovery of the wake velocity. Interestingly, this recovery is not significantly affected by the turbine loading although the amount of energy extracted from the flow strongly differs for the two load cases. The underlying reason for the accelerated wake velocity recovery

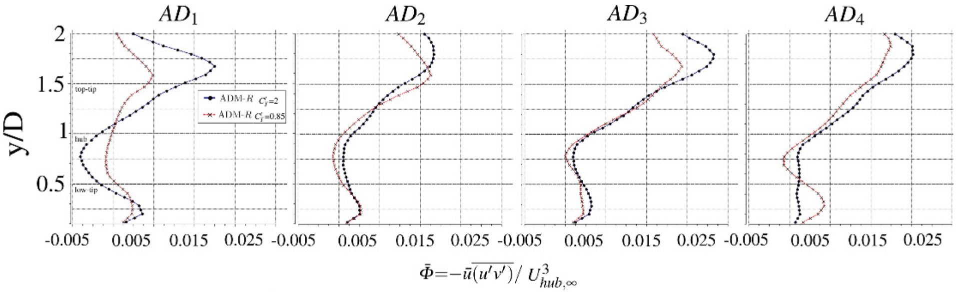

Fig. 8.7 Vertical profiles of the normalized vertical flux of mean flow kinetic energy $\overline{\Phi}$. The profiles are computed at turbine downstream locations $x/D = 5$

at higher turbine loading is the intensified mixing between the undisturbed wind field and the wind turbine canopy. This can be concluded from the profiles of the normalized vertical flux of mean flow kinetic energy $\overline{\Phi}$ depicted in Fig. 8.7 which show that for higher turbine loading the vertical momentum transport in the flow region above the turbines is increased significantly [8].

The power extracted by each turbine is calculated as $\overline{P} = T\overline{U}_\mathrm{d}$ with the thrust force T estimated from the surface integral of the mean static pressure immediately upstream and downstream of the actuator disks. Approximately 20% more power was extracted from the flow by the turbines under optimal loading conditions.

8.4 Numerical Simulations of a Wind Turbine Array with Kites

In this section we present simulation results for an array of four wind turbines, interspersed with kites which are modeled as distributed body forces. The domain size, inter-turbine spacing, type of actuator disk model, size, positioning and aerodynamic properties of the kites are kept constant for all evaluated cases. Each of the four kites has a total wing surface area of $A_\mathrm{k} = 470\,\mathrm{m}^2$, which corresponds to a relative size $A_\mathrm{k}/A_\mathrm{d} = 1/11$. A glide angle $\varepsilon = 10°$ is assumed, which, according to Fig. 8.4 (center) and Eq. (8.16), leads to a lift-to-drag ratio of $L/D = 5.67$. To model the interaction with the wind field the double-curved wing is geometrically simplified as a planar elliptical wing with a surface area equivalent to the projected area of the physical wing. Assuming an aspect ratio of $A\!\!\!R = 2$ the dimensions of the elliptical wing are calculated as 16×32 m. Each wing is placed at a vertical distance $D/4$ above and a horizontal distance $3D$ downstream of the corresponding actuator disk. The resulting configuration is illustrated in Fig. 8.8, indicating how several levels of mesh refinement are used to approximate the kite surfaces. The regions of mesh refinement are also shown in the top and isometric views. The elliptical wings can be recognized in the center of these regions.

As mentioned above the kites are not represented as solid flow boundaries, because this would require very fine meshes to resolve viscous boundary layers, but

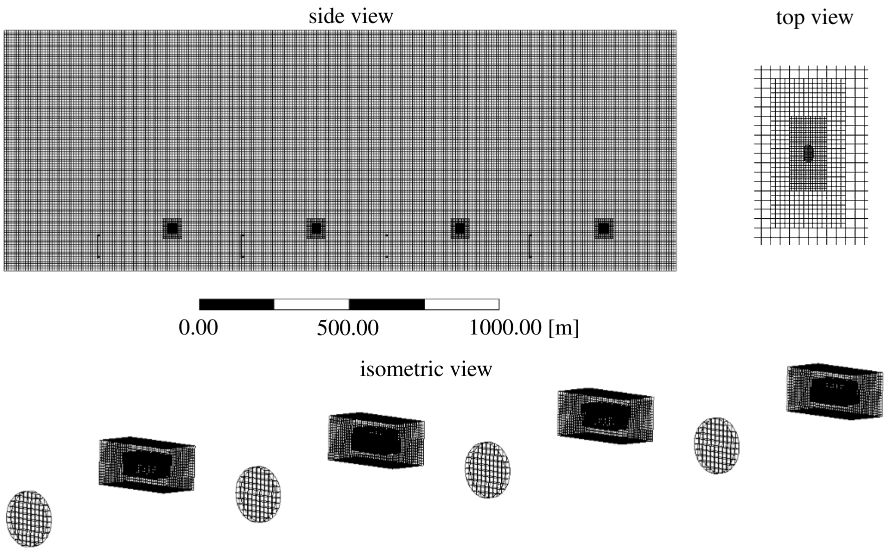

Fig. 8.8 Computational mesh of the flow domain showing several levels of refinement in the regions containing the kite surfaces. The hexahedral cells directly at the kite surface have a uniform side length of $\Delta x = 1$ m

instead are modeled as distributed body forces. These are generated by pressure jumps over infinitely thin surfaces, as derived from de Wachter [30]. The purpose of the local mesh refinement is to better approximate the desired surface area and eventually the total force on the flow (surface integral of static pressure). The four actuator discs (ADM-R) are modeled as circular infinitely thin surfaces without applying any local mesh refinement. The evaluated cases are summarized in Table 8.2.

Case	C'_T	β [°]	ΔP [Pa]	v_a [m/s]	F_a [kN]	P' [W/m^2]
(a)	0.85	80	39	7.8	18.5	307
(b)	2	80	39	7.8	18.5	307
(c)	2	75.7	79	11.1[a]	37	873[a]
(d)	2	69.7	157	15.6[a]	74	2456[a]

[a] Values that kites would experience for crosswind operation

Table 8.2 Simulation cases and parameter combinations for a wind turbine array with interspersed kites operating at $v_w = 7.8\,\mathrm{m/s}$. The kite power density is defined by Eq. (8.20) as $P' = F_a v_a / A_k$, using the listed values of F_a and v_a as well as $A_k = 470\,\mathrm{m}^2$

In cases (a) and (b) the kites are positioned statically and the effect of partial and optimal loading of the turbines, $C'_T = 0.85$ and 2, on the wake flow is studied. In cases (c) and (d) the turbines are operated at optimal loading and the effect of increasing kite power density on the wake flow is studied. To double the aerodynamic force of the individual kites and by that also the reaction forces acting on the flow from $F_a = 18.5\,\mathrm{kN}$ to $37\,\mathrm{kN}$ and in a second step further to $74\,\mathrm{kN}$ the kites are considered to perform crosswind flight maneuvers at lower elevation angles. To avoid the computationally demanding direct modeling of flight maneuvers the kites are positioned statically in the flow domain and the flow boundary condition at the wings is prescribed such that the aerodynamic force for true crosswind operation is reproduced. This is achieved by increasing the pressure jump ΔP across the wing surface from 39 Pa to 79 Pa and further to 157 Pa.

8.4.1 Effect of Varying Wind Turbine Load

In a first step, the effect of different wind turbine loading on the wake flow is investigated and compared to the reference cases without kites, presented in Figs. 8.6 and 8.7. Similar to these, a higher wind turbine loading is associated with increased energy extraction from the flow. Figure 8.9 shows that the resulting velocity deficit

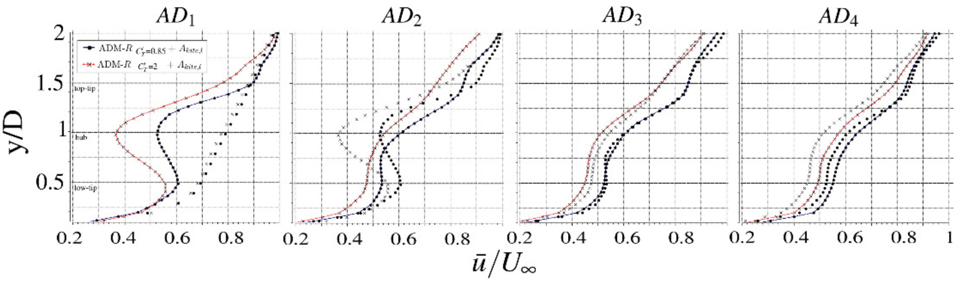

Fig. 8.9 Vertical profiles of the normalized streamwise velocity. The profiles represented by lines and symbols are computed at turbine downstream locations $x/D = 5$. The profiles represented only by symbols are computed at turbine upstream locations $x/D = -1$, with crosses denoting the load case $C_T' = 2$ and dots the load case $C_T' = 0.85$

in the wake of AD_1 is particularly pronounced for the case of higher turbine loading. Further downstream, the turbine wake flows approach an equilibrium state with less pronounced velocity differences. Wake velocity recovery for partial turbine loading stabilizes to about $0.6\overline{U}_{\infty,\mathrm{h}}$ and for optimal loading to about $0.5\overline{U}_{\infty,\mathrm{h}}$, where $\overline{U}_{\infty,\mathrm{h}}$ represents the mean free stream velocity at hub height. Interestingly, for the optimal turbine loading the introduction of kites does not affect the velocity recovery in the wakes of AD_3 and AD_4. However, for the partial loading the effect of the kites is much more pronounced and the wake velocity recovery is enhanced also for AD_4.

The profiles of the normalized vertical flux of mean flow kinetic energy $\overline{\Phi}$ are shown in Fig. 8.10. The diagrams indicate that the wind turbine loading does not significantly affect the vertical transport of momentum in the wakes of the actuator

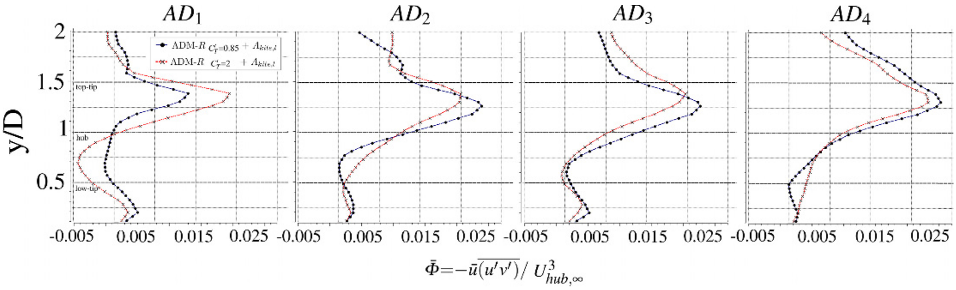

Fig. 8.10 Vertical profiles of the normalized vertical flux of mean flow kinetic energy $\overline{\Phi}$. The profiles are computed at turbine downstream locations $x/D = 5$

disks AD_2, AD_3 and AD_4. When compared to the reference cases shown in Fig. 8.7, the magnitude of the kinetic energy flux is on average four times larger in the wake region, independent of the load cases.

At partial loading of the turbines the use of kites increases the energy extraction from the flow by 14% and at optimal loading by 5.5%. Correspondingly, the turbine array efficiency increases by 8.2% and 2.5%, respectively. Because of the low efficiency gain at optimal loading we investigate the effect of increasing kite power density on the wake flow of the turbine array.

8.4.2 Effect of Varying Kite Power Density

To enhance the flow deflection towards the ground surface and, as consequence, to intensify the flow entrainment into the turbine canopy the kites are considered to perform crosswind flight maneuvers at decreased elevation angles. In this way, the resulting force per kite is doubled in two steps from $F_a = 18.5\,\text{kN}$, which is the value for static flight, to 37 kN and then to 74 kN, while operating the turbine at optimal loading and maintaining a constant wind velocity of $v_w = 7.8\,\text{m/s}$.

As illustrated in Fig. 8.8 the kites are represented as distributed body forces and are resolved by several levels of local mesh refinement. A direct modeling of flight maneuvers would substantially increase the complexity of the simulations. Because the main interest of this study is the integral force that the kites exert on the turbine wake flows we model the flying kites as static objects and adjust the flow boundary condition such that the prescribed force per kite, as listed in Table 8.2, is generated. Calculation basis of this approach, which is outlined in [22, Appendix C], is the discrete pressure distribution of a ram-air kite adopted from [30]. The integral aerodynamic force of each wing is determined from the discrete pressure distribution along its upper and lower surfaces according to Eq. (8.21). To reach the target values $F_a = 37\,\text{kN}$ and 74 kN we use an iterative procedure to determine the apparent velocities of $v_a = 11.1\,\text{m/s}$ and $15.6\,\text{m/s}$. The fan boundary condition in Fluent®is used with constant pressure jumps of $\Delta P = 79\,\text{Pa}$ and 157 Pa, respectively. Keep-

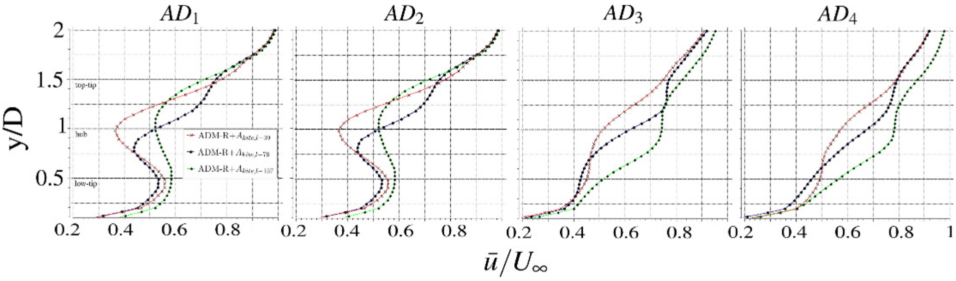

Fig. 8.11 Vertical profiles of the normalized streamwise velocity computed at turbine downstream locations $x/D = 5$ for the actuator disks under optimal load $C_T' = 2$. The three profiles show the effect of different kite power densities on the wake velocity. They are indexed by the different values of the pressure jump ΔP listed in Table 8.2

ing the glide angle $\varepsilon = 10°$ constant and, as consequence also the lift-to-drag ratio $L/D = 5.67$, the required values of the elevation angle β are calculated from Eq. (8.16) as $\beta = 75.7°$ and $69.7°$.

The influence of increasing kite power density on the wake velocity is illustrated in Fig. 8.11. As expected, a stronger deflection of the flow towards the ground surface also leads to a faster recovery of the wake velocity. Doubling the aerodynamic forces of the kites results in a 20% faster velocity recovery at the hub height $y/D = 1$ and downstream $x/D = 5$ of the actuator disks AD_3 and AD_4. Quadrupling the aerodynamic forces results in a 50% faster velocity recovery.

Interesting conclusions can be drawn from the normalized vertical flux of mean flow kinetic energy depicted in Fig. 8.12. The diagrams indicate that increased kite power densities intensify the fluctuations of the vertical momentum transport and as consequence expand the affected flow cross section. Similar trends are expected for the shear stress and the turbulence kinetic energy transport. For higher kite power densities, horizontal oscillations in the magnitude of vertical momentum flux are identified as regions of high turbulent kinetic energy production (oscillations above hub height) and dissipation (oscillations below hub height) which is shown to en-

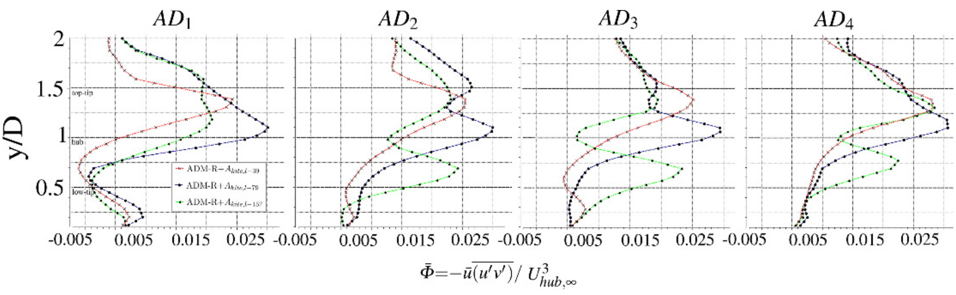

Fig. 8.12 Vertical profiles of the normalized vertical flux of mean flow kinetic energy $\overline{\Phi}$ computed at turbine downstream locations $x/D = 5$ for the actuator disks under optimal load $C_T' = 2$. The three profiles show the effect of different kite power densities

hance the re-energizing of the wake flow [32]. A significantly higher kinetic energy flux in the wake region is translated into more energy available for extraction by the downstream turbines.

At the maximum kite power density $P' = 2456\,\mathrm{W/m^2}$, a 24% increase in power production and a 15% increase in conversion efficiency is predicted compared to the base case. The use of kites with power density $P' = 873\,\mathrm{W/m^2}$ results in a 12% increase of extracted power and a conversion efficiency increase of approximately 10% relative to the base case.

8.5 Conclusions

The presented computational study investigates the flow entrainment effect of large kites on the operational characteristics of a conventional wind farm. The considered farm configurations are simplified and many practical aspects concerning the flight operation of kites and wind turbine control schemes are neglected. The large eddy simulations clearly show that the positioning of tethered wings within the wind turbine array significantly affects the spatial distribution of the mean velocity deficit and the vertical kinetic energy flux in the turbine wake flows. The stronger the traction forces of the kites and, accordingly, the reaction forces acting on the flow above the wind turbine canopy, the higher the vertical kinetic energy flux, the faster the wake velocity recovery and the higher the energy extraction efficiency of the wind farm. In all investigated cases the highest values of the turbulent flux are found in the upper regions of the wake flows where the mean shear is maximum. This finding is in line with existing literature [32]. Due to the promising results it is expected that further studies will investigate the effect of altering the wake flow characteristics using downwash-generating devices such as kites.

Acknowledgements The authors would like to thank the anonymous reviewers for their helpful comments and gratefully acknowledge the contribution of Dhruv Mehta and Lorenzo Lignarolo for their expert advice on the wide range of topics treated in the present work.

References

1. Ahmed, M., Hably, A., Bach, S.: High Altitude Wind Power Systems: A Survey on Flexible Power Kites. In: Proceedings of the 2012 XXth International Conference on Electrical Machines, pp. 2085–2091, Marseille, France, 2–5 Sept 2012. doi: 10.1109/ICElMach.2012.6350170
2. Ammara, I., Leclerc, C., Masson, C.: A viscous three-dimensional differential/actuator-disk method for the aerodynamic analysis of wind farms. Journal of Solar Energy Engineering **124**(4), 345–356 (2002). doi: 10.1115/1.1510870
3. Annoni, J., Seiler, P., Johnson, K., Fleming, P., Gebraad, P.: Evaluating wake models for wind farm control. In: Proceedings of the 2014 American Control Conference, pp. 2517–2523, IEEE, Portland, OR, USA, 4–6 June 2014. doi: 10.1109/ACC.2014.6858970

4. Barthelmie, R. J., Hansen, K., Frandsen, S. T., Rathmann, O., Schepers, J. G., Schlez, W., Phillips, J., Rados, K., Zervos, A., Politis, E. S., Chaviaropoulos, P. K.: Modelling and measuring flow and wind turbine wakes in large wind farms offshore. Wind Energy **12**(5), 431–444 (2009). doi: 10.1002/we.348
5. Bitar, E., Seiler, P.: Coordinated control of a wind turbine array for power maximization. In: Proceedings of the 2013 American Control Conference, pp. 2898–2904, IEEE, Washington, DC, USA, 17–19 June 2013. doi: 10.1109/ACC.2013.6580274
6. Boonman, D., Broich, C., Deerenberg, R., Groot, K., Hamraz, A., Kalthof, R., Nieuwint, G., Schneiders, J., Tang, Y., Wiegerink, J.: Wind Farm efficiency. S12, Delft University of Technology, Delft, Netherlands, 2011. http://resolver.tudelft.nl/uuid:9ec5078c-c02a-43db-99b9-00bde8871b58
7. Burton, T., Jenkins, N., Sharpe, D., Bossanyi, E.: Wind Energy Handbook. 2nd ed. John Wiley & Sons, Ltd, Chichester (2011). doi: 10.1002/9781119992714
8. Cal, R. B., Lebrón, J., Castillo, L., Kang, H. S., Meneveau, C.: Experimental study of the horizontally averaged flow structure in a model wind-turbine array boundary layer. Journal of Renewable and Sustainable Energy **2**(1), 013106 (2010). doi: 10.1063/1.3289735
9. Calaf, M., Meneveau, C., Meyers, J.: Large eddy simulation study of fully developed wind-turbine array boundary layers. Physics of Fluids **22**, 015110 (2010). doi: 10.1063/1.3291077
10. Castro, I.: CFD for external aerodynamics in the built environment. The QNET-CFD Network Newsletter **2**(2), 4–7 (2003)
11. DNV GL: Wind farm design tool WindFarmer. https://www.dnvgl.com/services/windfarmer-3766. Accessed 1 Nov 2016
12. Dobrev, I., Massouh, F., Rapin, M.: Actuator surface hybrid model. In: Journal of Physics: Conference Series, vol. 75, 1, p. 012019, (2007). doi: 10.1088/1742-6596/75/1/012019
13. DTU Wind Energy: Wind Atlas Analysis and Application Program (WAsP). http://www.wasp.dk/. Accessed 1 Nov 2016
14. EMD International A/S: Software package windPRO. http://www.emd.dk/windpro/. Accessed 1 Nov 2016
15. Fritz, F.: Application of an Automated Kite System for Ship Propulsion and Power Generation. In: Ahrens, U., Diehl, M., Schmehl, R. (eds.) Airborne Wind Energy, Green Energy and Technology, Chap. 20, pp. 359–372. Springer, Berlin Heidelberg (2013). doi: 10.1007/978-3-642-39965-7_20
16. Jarrin, N., Benhamadouche, S., Addad, Y., Laurence, D.: Synthetic turbulent inflow conditions for large eddy simulation. In: Proceedings of the 4th International Turbulence, Heat and Mass Transfer Conference, Antalya, Turkey, 12–17 Oct 2003
17. Jimenez, A., Crespo, A., Migoya, E., Garcia, J.: Advances in large-eddy simulation of a wind turbine wake. In: Journal of Physics: Conference Series, vol. 75, p. 012041, (2007). doi: 10.1088/1742-6596/75/1/012041
18. Loyd, M. L.: Crosswind kite power. Journal of Energy **4**(3), 106–111 (1980). doi: 10.2514/3.48021
19. Madsen, H. A.: A CFD analysis of the actuator disc flow compared with momentum theory results. In: Proceedings of the 10th IEA Symposium on the Aerodynamics of Wind Turbines, pp. 109–124, Edinburgh, UK, 16–17 Dec 1996
20. Meyers, J., Meneveau, C.: Large eddy simulations of large wind-turbine arrays in the atmospheric boundary layer. AIAA Paper 2010-827. In: Proceedings of the 48th AIAA Aerospace Sciences Meeting, Orlando, FL, USA, 4–7 Jan 2010. doi: 10.2514/6.2010-827
21. Meyers, J., Meneveau, C.: Optimal turbine spacing in fully developed wind farm boundary layers. Wind Energy **15**(2), 305–317 (2012). doi: 10.1002/we.469
22. Ploumakis, E.: Improving the Wind Farm efficiency by simple means – LES study of a wind turbine array with tethered kites. M.Sc.Thesis, Delft University of Technology, 2015. http://resolver.tudelft.nl/uuid:a273b26a-b4bd-4388-8eee-193c6d22626b
23. Ploumakis, E., Mehta, D., Lignarolo, L., Bierbooms, W.: Enhanced Kinetic Energy Entrainment in Wind FarmWakes – LES Study of a Wind Turbine Array with Tethered Kites. In: Schmehl, R. (ed.). Book of Abstracts of the International Airborne Wind Energy Conference

2015, p. 52, Delft, The Netherlands, 15–16 June 2015. doi: 10.4233/uuid:7df59b79-2c6b-4e30-bd58-8454f493bb09. Presentation video recording available from: https://collegerama.tudelft.nl/Mediasite/Play/383929c21f734297ba296717de3d17371d
24. Schmehl, R., Noom, M., Vlugt, R. van der: Traction Power Generation with Tethered Wings. In: Ahrens, U., Diehl, M., Schmehl, R. (eds.) Airborne Wind Energy, Green Energy and Technology, Chap. 2, pp. 23–45. Springer, Berlin Heidelberg (2013). doi: 10.1007/978-3-642-39965-7_2
25. Smirnov, A., Shi, S., Celik, I.: Random flow generation technique for large eddy simulations and particle-dynamics modeling. Journal of Fluids Engineering **123**(2), 359–371 (2001). doi: 10.1115/1.1369598
26. Stevens, R. J. A. M., Gayme, D. F., Meneveau, C.: Effects of turbine spacing on the power output of extended wind-farms. Wind Energy **19**(2), 359–370 (2016). doi: 10.1002/we.1835
27. Stevens, R. J. A. M., Gayme, D. F., Meneveau, C.: Large eddy simulation studies of the effects of alignment and wind farm length. Journal of Renewable and Sustainable Energy **6**(2) (2014). doi: 10.1063/1.4869568
28. Troldborg, N.: Actuator line modeling of wind turbine wakes. Ph.D. Thesis, Technical University of Denmark, 2009. http://orbit.dtu.dk/files/5289075/niels_troldborg.pdf
29. Troldborg, N., Sorensen, J. N., Mikkelsen, R.: Actuator Line Simulation of Wake of Wind Turbine Operating in Turbulent Inflow. Journal of Physics: Conference Series **75**, 012063 (2007). doi: 10.1088/1742-6596/75/1/012063
30. Wachter, A. de: Deformation and Aerodynamic Performance of a Ram-Air Wing. M.Sc.Thesis, Delft University of Technology, 2008. http://resolver.tudelft.nl/uuid:786e3395-4590-4755-829f-51283a8df3d2
31. Wright, N. G., Easom, G. J.: Non-linear k-ε turbulence model results for flow over a building at full-scale. Applied Mathematical Modelling **27**(12), 1013–1033 (2003). doi: 10.1016/S0307-904X(03)00123-9
32. Wu, Y.-T., Porté-Agel, F.: Atmospheric turbulence effects on wind-turbine wakes: An LES study. Energies **5**(12), 5340–5362 (2012). doi: 10.3390/en5125340
33. Wu, Y.-T., Porté-Agel, F.: Simulation of turbulent flow inside and above wind farms: Model validation and layout effects. Boundary-layer meteorology **146**(2), 181–205 (2013). doi: 10.1007/s10546-012-9757-y